Chem

CellPress

Chem

Article

Mixed proton-electron conductivity in a dynamic 3D metal-organic framework

Graphical abstract

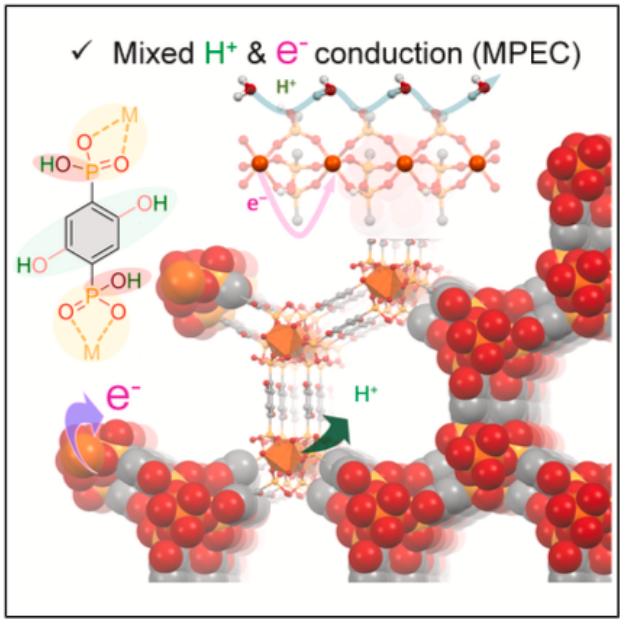

Authors

Darsi Rambabu, Tom Goossens, Vasudeva Rao Bakuru, ..., Yaroslav Filinchuk, Benoît Champagne, Alexandru Vlad

Correspondence

alexandru.vlad@uclouvain.be

In brief

A family of breathable phosphonate-based 3D MOFs with mixed conduction is explored. Metal-phosphonate nodes and uncoordinated phosphonate (P-OH) groups enable dynamic structure and proton conductivity, assisted by ordered water channels. Comparative studies with an Al-MOF, showing only proton conductivity, highlight iron's role in enabling dual proton-electrical conductivity. Uncoordinated hydroquinone adds to multifunctionality through reversible redox behavior.

Highlights

- Breathable 3D MOF with mixed proton-electron conductivity
- Metal-phosphonate nodes and uncoordinated phosphonates enable proton conduction
- Water channels support dynamic structural adaptability
- Uncoordinated hydroquinone groups induce redox functionality

This manuscript is a preprint of an article published in *Chem Journal, CelPress.*

DOI : 10.1016/j.chempr.2025.102590

The final authenticated version is available online at :

https://doi.org/10.1016/j.chempr.2025.102590

Chem

CellPress

Article

Mixed Proton-Electron Conductivity in a Dynamic 3D Metal-Organic Framework

Darsi Rambabu,[1] Tom Goossens,[1] Vasudeva Rao Bakuru,[1] Petru Apostol,[1] François Mairesse,[2] Timothy Steenhaut,[1] Pierre Beaujean,[2] Soumya Kanti Mondal,[3] Xiaolong Guo,[1] Yan Zhang,[1] Shubhadeep Pal,[1] Robert Markowski,[1] Xiaodong Lin,[1] Pan Xu,[4] Géraldine Chanteux,[1] Andrii Kachmar,[1] Da Tie,[1] Augustin Ramackers,[1] Viliam Frano,[1] Koen Robeyns,[1] Tapas Kumar Maji,[3] Yaroslav Filinchuk,[1] Benoît Champagne,[2] Alexandru Vlad[1,] *

[1]Institute of Condensed Matter and Nanosciences, Molecular Chemistry, Materials and Catalysis, Université catholique de Louvain, Louvain-la-Neuve B-1348, Belgium

[2]Unité de Chimie Physique Théorique et Structurale, Chemistry Department, Namur Institute of Structured Matter, University of Namur, Belgium

[3]Molecular Materials Laboratory, Chemistry and Physics of Material Unit (CPMU), School of Advance Material (SAMat), Jawaharlal Nehru Centre for Advanced Scientific Research, Jakkur, Bangalore, 560064, India

[4] China State Key Laboratory of Physical Chemistry of Solid Surfaces, Department of Chemistry, College of Chemistry and Chemical Engineering, Xiamen University, 361005, Xiamen, China.

Email: alexandru.vlad@uclouvain.be

SUMMARY

Metal-organic frameworks (MOFs) with mixed proton and electron conductivity (MPEC) are promising materials for electrochemical energy systems, yet few examples merge these properties within a single phase. Here, we report a series of breathable 3D MOFs featuring mixed conduction with the general formula H_{12}-M_2-(DOBDP)$_3$ [wherein M(III) = Fe, Al, Sc, In; and H_6-DOBDP = 2,5-dihydroxy-1,4-benzenediphosphonic acid]. The metal-phosphonate nodes and uncoordinated phosphonate (P-OH) groups enable the structure dynamics as well as proton conductivity, assisted by water channels. High proton conductivity (1.6×10^{-4} S/cm) and moderate electron conductivity (8.3×10^{-7} S/cm) are measured for the hydrated state of the Fe MOF phase, whereas the Al-phase exhibits only proton conductivity, highlighting the critical role of the Fe center in enabling MPEC. These findings advance the understanding of dual-conductive MOFs and establish a framework for designing next-generation materials with combined ion and electron transport.

Mixed proton-electron conduction, Dual-conductors, metal-organic framework, muti-metallic, Breathing behavior, water adsorption.

INTRODUCTION

The rising demand for efficient energy storage and conversion systems emphasizes the importance of mixed proton and electron conducting (MPEC) materials in electrochemical applications including fuel cells, batteries, chemical separation membranes and electrocatalysts.[1–3] Incorporating MPEC materials as electrodes in fuel cells or proton batteries enhances efficiency by facilitating rapid mass and charge transport, maximizing energy conversion.[2] Traditional physical blending methods for MPECs have limitations, often resulting in poorly defined structures and inefficient transport limited by percolation.[4,5] Recent studies have shown promise with perovskite and graphene oxide composites, but their ambiguous structure pose challenges in establishing a clear structure-property relationship.[6,7] To advance this field and overcome the limitations of physical blending, it is thus essential to develop well-defined, single-phase MPEC materials.

THE BIGGER PICTURE

Electrochemical technologies are at the heart of a sustainable energy future, powering innovations from clean energy storage to next-generation fuel cells. A challenge in this field has been finding materials that can efficiently transport both protons and electrons — key to many energy conversion and storage processes. Enter metal-organic frameworks (MOFs): highly tunable materials with immense potential, but typically limited to either proton or electron conduction. Herein, we are introducing a dynamic, breathable 3D MOF that combines both proton and electron conductivity within a single phase. The secret lies in its reversible structural transformation, driven by water interactions and uncoordinated functional groups, which enable seamless dual conduction. This advance not only redefines the boundaries of MOF functionality but also opens the door to entirely new design strategies for materials at the intersection of chemistry, physics, and energy science.

Metal-organic frameworks (MOFs) have gained traction for their potential in electron or proton conduction processes.[8–10] Electrical conductivity in MOFs originates from the overlap of d-p orbitals between metal nodes and organic linkers. Proton conductivity, on the other hand, is often achieved by introducing functionalities on linkers or unsaturated metal nodes, enhancing pore hydrophilicity, and enabling long-range proton migration through hydrogen bonding networks.[8] While MOFs have shown either proton or electron conduction, combining both in a single 2D- or 3D-MOF system remains poorly explored[11–14] Notable examples include In(III)-tetrathiafulvalene,[11] 2D Zn-HHTP-H_2O,[12] and TTFTP-La[14] MOF systems, all shown to exhibit simultaneous electron and proton conduction.

Recently, we explored the ionic conductivity and redox activity of the MOF A_4-Zn-DOBDP (A = Li, Na, H_6-DOBDP = 2,5-dihydroxy-1,4-benzenediphosphonic acid) positive electrode; however, this phase was found to be electrically insulating.[15] In this context, we considered the hexa-anionic phosphono-phenolate linker (H_6-DOBDP) with the aim of constructing the MOF by incorporating Ar-PO_2^- groups with a redox-active metal ion (*e.g.* Fe). This combination can facilitate electronic conduction, while the presence of P-OH and Ar-OH (hydroquinone/phenolate) groups can be responsible for proton conductivity and redox activity, respectively (**Scheme 1**).

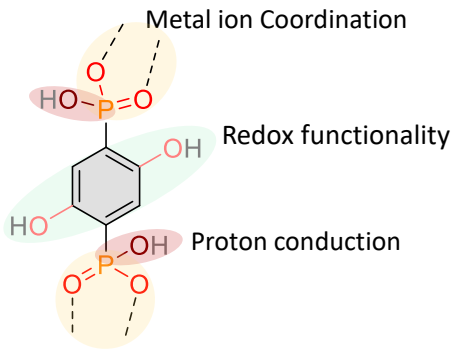

Scheme 1. Design strategy for the MOF

Emphasizing on coordination and charge balance sites (Ar-PO^{2-}), non-coordinated phosphonate (HO-P) for proton conductivity, and hydroquinone redox center.

Herein, we present a series of MOFs based on phosphono-phenolate linker, denoted hereafter as H_{12}-M_2-(DOBDP)$_3$, wherein M = Fe^{3+}, Al^{3+}, Sc^{3+}, In^{3+}; and H_6-DOBDP = 2,5-dihydroxy-1,4-benzenediphosphonic acid. A mixed tetra-metallic H_{12}-$Fe_xAl_ySc_zIn_a$-(DOBDP)$_3$ composition was also prepared, which is noteworthy due to its multi-metal ion composition in a single system, potentially leading to diverse properties.[16] Particularly, Fe and Al systems are found to exhibit reversible structural breathing behavior[17–21] upon dehydration and re-hydration in the crystalline state and the process is studied experimentally and theoretically in detail. Fully hydrated and partially dehydrated phases of the H_{12}-Fe_2-(DOBDP)$_3$ are found to be efficient MPECs, with the highest proton and electrical conductivities of 1.6×10^{-4} S cm^{-1} and 8.7×10^{-7} S cm^{-1}, respectively, at 293 K and ambient conditions. Furthermore, reversible hydroquinone ↔ quinone transformations in Al- and Fe-MOFs are observed through reversible chemical oxidation-reduction and electrochemical solid-state cyclic voltammetry analysis, demonstrating the redox activity.

RESULTS and DISCUSSION

Synthesis and physicochemical analysis of H_{12}-M_2-DOBDP$_3$ [M = Fe, Al, Sc, In] MOFs

Single crystals of the H_{12}-M_2-(DOBDP)$_3$ (M = Fe, Al) MOFs were obtained by reacting H_6-DOBDP and Fe(II) or Al(III) salts, in water, at 70°C for 48h, or at room temperature for 2 years, respectively. Bulk powder phases of H_{12}-M_2-(DOBDP)$_3$ MOFs were typically synthesized by reacting 3 equivalents of H_6-DOBDP with 2 equivalents of the corresponding metal salts at 40°C, in aqueous solution (refer to the Experimental Procedures for details).

The single crystal X-ray diffraction (XRD) analysis revealed a porous hexagonal structure (honeycomb type) for the H_{12}-M_2-(DOBDP)$_3$ (M= Fe, Al). Both frameworks crystallize in the trigonal *P-3c1* space group, with the trivalent metal nodes octahedrally coordinated to six phosphonates groups from different H_4-DOBDP^{2-} linkers [denoted as M(O_2P-OH)$_6$]. Neighboring metal nodes are interconnected by three bridging phosphonate linkers, forming 1D chain-like secondary building units (SBUs) of [Fe(O_2P-OH)$_3$]$_n$ along the *c*-axis (**Figures 1 and S3**). The 1D chain SBUs are interconnected by the H_4-DOBDP^{2-} linker, generating a 3D framework displaying hexagonal channels (~13Å wide), along the *c*-axis. The channels in the as prepared Fe-MOF are found to be filled with 21 guest water molecules, with a net composition of H_{12}-Fe_2-(DOBDP)$_3$·21H_2O (**Figures 2, and S4**, denoted hereafter as H_{12}-Fe_2-(DOBDP)$_3$_sh (sh standing for super-hydrated). In contrast, the localization of water molecules in Al-MOF (6 per formula unit) was not possible due to higher disorder. The structures are charge-neutral, with for instance two M(III) cations and three anionic H_4-DOBDP^{2-} linkers per each formula unit (H_{12}-M_2-(DOBDP)$_3$). The remaining 12 protons (6 from phenolic and 6 from phosphonate units) suggests significant potential for proton conduction and redox activity (the hydroquinone).[15,22]

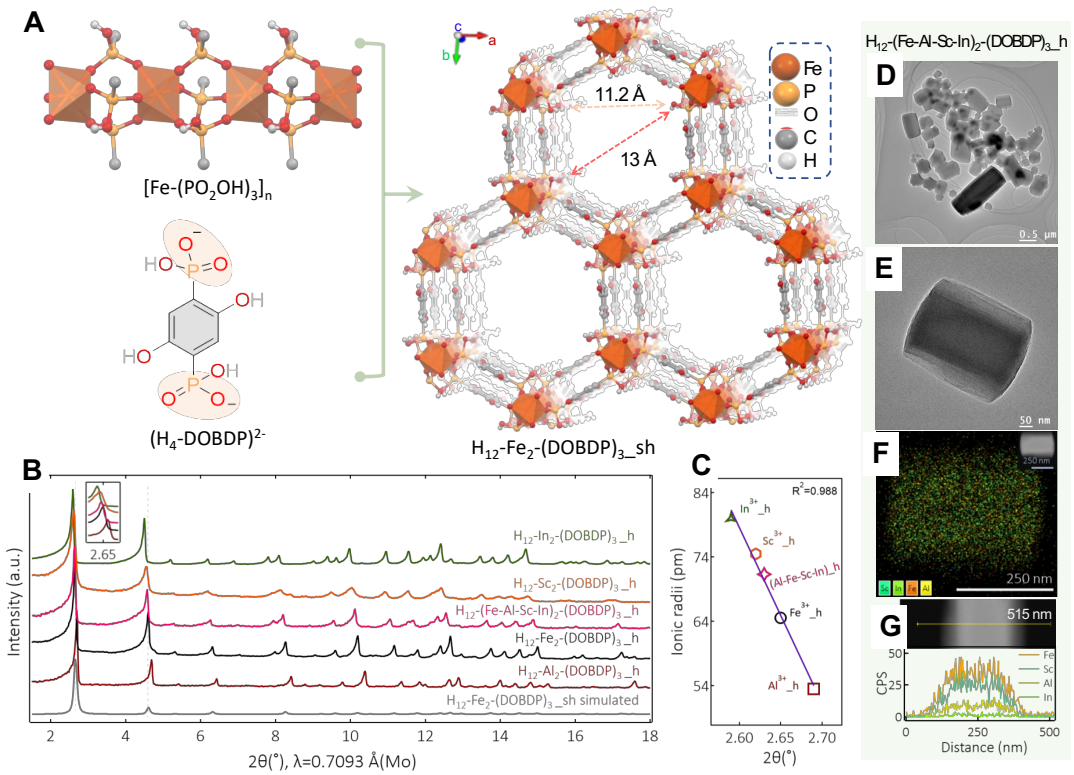

Figure 1. Structural analysis of H_{12}-M_2-(DOBDP)$_3$ MOFs

(A) Crystal structure of H_{12}-Fe_2-(DOBDP)$_3$ MOF highlighting the $[Fe(O_2P\text{-}OH)_3]_n$ 1D-chain and linker (to the left), with the view along *c*-axis to the right (water molecules omitted for clarity).

(B) Powder XRD patterns of the five isostructural Al-, Fe-, Sc-, In-monometallic, and (Fe-Al-Sc-In)-tetrametallic MOFs.

(C) Correlation between the ionic radii of the metal cations and the 2**θ** position of the main diffraction peak (*hkl* = *100*); ionic radii: Al^{3+} 53.5 pm < Fe^{3+} 64.5 pm < $Fe_{0.31}Al_{0.06}Sc_{0.44}In_{0.19}$ Avg. 71.2 pm < Sc^{3+} 74.5 pm < In^{3+} 80 pm.

(D) low and (E) high magnification TEM images of H_{12}-(Fe-Al-Sc-In)$_2$-(DOBDP)$_3$ MOF particles, with (F) the EDX elemental mapping showing uniform distribution of the elements.

(G) EDX line profile of the elements of the tetrametallic MOF, H_{12}-(Fe-Al-Sc-In)$_2$-(DOBDP)$_3$.

All H_{12}-M_2-DOBDP$_3$_h [M = Fe, Al, Sc, In; h refers to the hydrated] MOFs were found to exhibit hexagonal crystallites with size around 300 nm (**Figure S5**), with the XRD patterns similar to that of the Fe(III) homologue (H_{12}-Fe_2-DOBDP$_3$_sh), confirming the phase purity and isostructurality (**Figure 1B**). This also evidence that the MOF structure remains unchanged, even though H_{12}-M_2-DOBDP$_3$_h MOFs contain 12 and 18 water molecules per formula, compared to the initial 21 (_sh), corresponding to the loss of 9 and 3 water molecules for Al/Fe-MOF and Sc/In-MOF, respectively (**Table 1**). A shift of the main diffraction peak (*hkl* = *100*) toward higher 2**θ** values

(±0.1°) is nevertheless observed, progressing from In_h to Al_h, which correlates linearly with the ionic radii of metal cations (**Figure 1C**), corroborating partial contraction or expansion of the lattice as function of the cation size.[23] Owing to the isostructural phases attained, a tetrametallic derivative, H_{12}-(Fe,Al,Sc,In)$_2$-DOBDP$_3$ was also prepared from a quaternary mixture composed of a 25% molar content of each metal precursor. This multimetallic composition is significant from a material standpoint, as such combinations can potentially impart multiple properties due to the presence of various metals, or reduce the quantity of a given metal for same amount and surface area MOF.[16,24] The tetrametallic MOF displays the same hexagonal rod-like morphology as its monometallic counterparts (**Figures 1D, E** and **S5D**) and an identical XRD pattern (**Figure 1B**), indicating isostructural materials. The energy-dispersive X-ray spectroscopy (EDX) mapping revealed uniform distribution of the four metal ions throughout the MOF crystallites (**Figure 1F**), despite a higher content of Fe and Sc as compared to Al and In (**Figure 1G**). This was also confirmed by inductively coupled plasma-optical emission spectrometry (ICP-OES) analysis wherein the composition of H_{12}-($Fe_{0.31}Al_{0.06}Sc_{0.44}In_{0.19}$)$_2$-(DOBDP)$_3$ was determined. Also, similar to the monometallic MOFs, the shift in the main diffraction peak (*hkl = 100*) correlates linearly with the estimated average ionic radii of the four metal cations (71.2 pm for $Fe_{0.31}Al_{0.06}Sc_{0.44}In_{0.19}$), confirming the presence of mixed metals composition, and in agreement with the estimated composition (**Figure 1C**). The preferential incorporation is likely due to differences in reaction kinetics and thermodynamic aspects, such as binding affinities between the metal ions and ligand.[25]

Water sorption and structure dynamics of H_{12}-Fe_2-(DOBDP)$_3$·21H_2O MOF

The as prepared MOFs where all found to contain structural water, with the content depending on the nature of the M cation. Upon extended analysis, the Fe-version revealed as most peculiar, with the structural changes and properties detailed in the following. The crystal structure of H_{12}-Fe_2-(DOBDP)$_3$·21H_2O (_sh) highlights the presence of nine sets of hydrogen bonding interactions, shaping a network within the framework (**Figures 2, S4**, and **Table S3**). Within the pores, a dense network is established by O11, O12, O13 and O14, each contributing four hydrogen bonds and forming a total of seven sets of intermolecular hydrogen bonds between water and water-phosphonate groups (e.g. H_2O···H-OH; O_2P-OH···OH_2; O_2P-HO···H-OH) (**Figures 2B, S4A,** and **Table S3**). This intricate hydrogen bonds network stabilizes the hexagonal framework and creates protonic transport channels along the *c*-axis, as detailed next (**Figure 2B**).

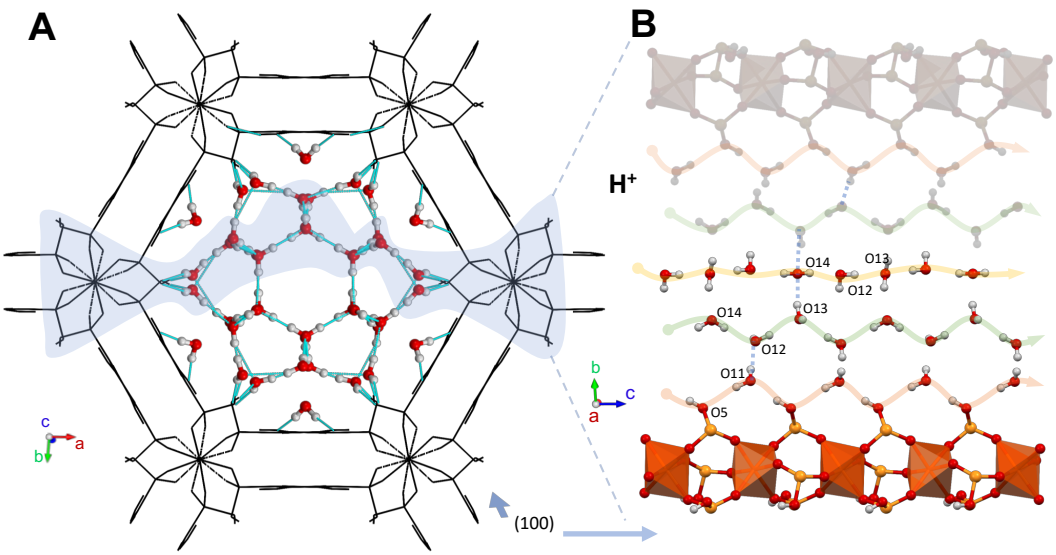

Figure 2. Hydrogen bond network in H_{12}-Fe_2-$(DOBDP)_3$·$21H_2O$ (_sh) MOF

(A) Water molecules organization and hydrogen bonding network as viewed along the *c*-axis.

(B) Proton channel formed by water molecules along the $[Fe(O_2P\text{-}OH)_3]_n$ 1D-chain.

Although the crystallographic structure derived from single crystal analysis indicates a composition of 21 molecules of H_2O per H_{12}-Fe_2-$(DOBDP)_3$ formula unit (**Figures 2 and S4**), thermogravimetric (TGA) and elemental (C, H) analyses (**Figure S6** and **Table 1, S1**) revealed a lower water content, due to the rapid loss of water during MOF separation from the synthesis medium. TGA revealed the presence of 12 water molecules for the Fe- and Al- compositions, and 18 H_2O molecules for the Sc- and In- versions. The TGA also revealed that complete dehydration is possible, occurring around 150°C (**Figure S6**), with these MOFs being stable up to 280°C. In situ (**Figure S7A, S8A**) and ex situ (**Figure 3A, S7B, S8B, S9**) XRD analysis was next employed to assess structural changes during the dehydration – rehydration process. For instance, the H_{12}-Fe_2-$(DOBDP)_3$·$12H_2O$ phase (_h,) underwent a three-steps structural change upon dehydration, leading progressively to H_{12}-Fe_2-$(DOBDP)_3$_ph (ph = partially hydrated, $7H_2O$), H_{12}-Fe_2-$(DOBDP)_3$_pd (pd = partially dehydrated, $3H_2O$), to fully dehydrated H_{12}-Fe_2-$(DOBDP)_3$_d upon heating to 250 °C under vacuum.

The analysis indicate that the H_{12}-Fe_2-$(DOBDP)_3$_d phase is closely isostructural to the hydrated phase, H_{12}-Fe_2-$(DOBDP)_3$_h (**Figures 3A, S7**). A similar behavior is noted for Al- composition, which exhibited a reversible two-phase change upon dehydration, with one intermediate and isostructural to Fe_ph analogue identified (**Figure 3A, S8, S9**). The H_{12}-Fe_2-$(DOBDP)_3$_pd appears to be a meta-stable phase, observed under inert conditions reverting immediately to H_{12}-Fe_2-$(DOBDP)_3$_ph upon exposure to ambient or humid air. The phase transition between hydrated and dehydrated forms of H_{12}-Fe_2-$(DOBDP)_3$ [e.g., hydrated (_h) ↔ partially hydrated (_ph) ↔ partially dehydrated (_pd) ↔ dehydrated (d)] was found to be reversible using ex-situ XRD (**Figure S9**). In contrast, Sc and In compositions were found to exhibit different phase change during dehydration process, with the In-MOF displaying irreversible changes after rehydration; while, rehydration of Sc-MOF is not straightforward, requiring heating to 70°C (**Figure S9**).

The process was also monitored by FTIR (**Figure S10**). The pristine MOFs display the (H-O-H) band positioned at 1625±4 cm^{-1}, which gradually disappeared upon dehydration, confirming the complete removal of guest water molecules from the MOFs. The slight shift of the phosphonate, phenolate, and aromatic bands, suggests that MOFs undergo structural distortion upon the dehydration, consistent with the structural changes as noted from the XRD experiments. The elemental (C, H) analysis estimated the water content in the MOF phases (refer to experimental section and **Table 1, Table S1**), revealing eight, seven, three and zero water molecules for H_{12}-Al_2-$(DOBDP)_3$_ph, H_{12}-Fe_2-$(DOBDP)_3$_ph, H_{12}-Fe_2-$(DOBDP)_3$_pd, and H_{12}-$(Fe/Al)_2$-$(DOBDP)_3$_d, respectively. In contrast, the water content in H_{12}-$(Sc/In)_2$-$(DOBDP)_3$_ph and H_{12}-$(Sc/In)_2$-$(DOBDP)_3$_d was found to be four and zero water molecule per formula unit, respectively (**Table 1**).

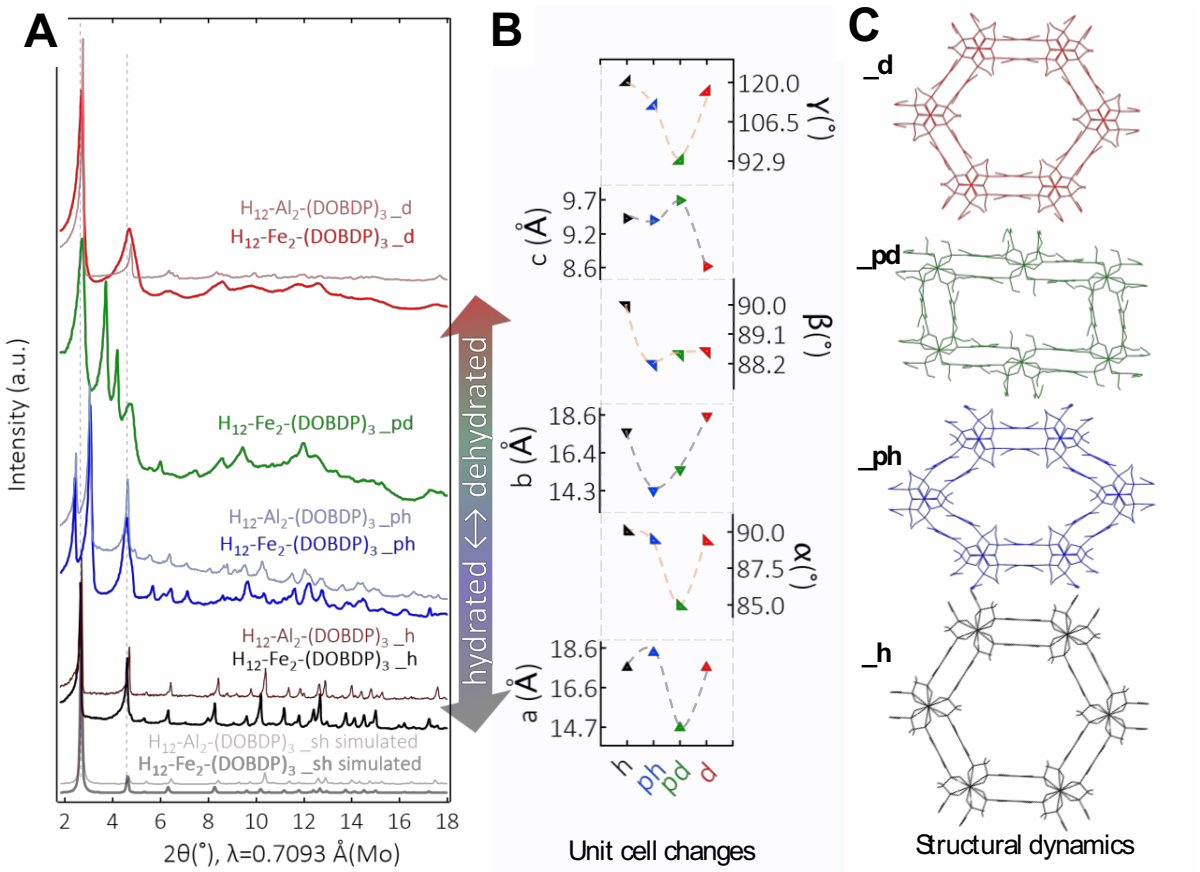

Figure 3. Breathing behavior of H_{12}-M_2-$(DOBDP)_3$ [M=Fe and Al] MOFs upon dehydration and rehydration

(A) XRD patterns of the stable phases during the dehydration of H_{12}-M_2-$(DOBDP)_3$ MOFs.

(B) The corresponding unit cells (a – b – c, α – β –γ) distortion for H_{12}-Fe_2-$(DOBDP)_3$ (_ph, _pd, and _d).

(C) *c*-axis views of the dynamic structural changes upon dehydration.

Table 1. Estimated water content in H_{12}-M_2-(DOBDP)$_3$ MOFs

MOF phase	X H_2O, X=	MOF phase	X H_2O, X=	MOF phase	X H_2O, X=
H_{12}-Fe_2-(DOBDP)$_3$_sh	21	H_{12}-(Sc/In)$_2$-(DOBDP)$_3$_h	18	H_{12}-(Sc/In)$_2$-(DOBDP)$_3$_ph	4
H_{12}-Al_2-(DOBDP)$_3$_sh	15$^+$	H_{12}-Fe_2-(DOBDP)$_3$_ph	7	H_{12}-Fe_2-(DOBDP)$_3$_pd	3
H_{12}-(Fe/Al)$_2$-(DOBDP)$_3$_h	12	H_{12}-Al_2-(DOBDP)$_3$_ph	8	H_{12}-M_2-(DOBDP)$_3$_d	0

$^+$ *indicates the remaining 6 water molecules cannot be located due to disorder in single crystal XRD data; sh = super hydrated, h = hydrated, ph= partial hydrated, ph= partial dehydrated, d= dehydrated*

Hydrogen bonding between water and the phosphonate/phenolate moieties are expected to play an integral role in the phase transitions of the Al and Fe MOFs, driving the reversible (de)hydration process (**Figure S9**). However, the precise localization of water molecules and the associated hydrogen-bond network was only attained for the (H_{12}-Fe_2-(DOBDP)$_3$_sh phase (**Figure 2**). To investigate thus the framework dynamics/breathing during the entire (de)hydration process, unit cell parameters of the intermediate phases were estimated from powder XRD data analysis (**Figure S11, Table S4**) and used to simulate the corresponding structures. During the initial stages of dehydration, H_{12}-Fe_2-(DOBDP)$_3$ undergoes noticeable elongation or contraction along the *a*- and *b*-axis (**Figure 3B, S12**). The hydrated _h phase, with a perfect hexagonal framework, progressively turned to a distorted hexagonal and subsequently into a rectangular framework (**Figure 3C**, _h ↔ _ph ↔ _pd). Whereas the hexagonal topology was recovered back upon complete dehydration (_d, **Figure 3C, S12**). This reversible structural transformation, termed breathing behavior,[18–21] is driven by the rearrangement of the water hydrogen-bond network, causing distortions in the framework (**Figure 2C, Figure S12**) and resulting in changes in unit cell parameters (**Figure 3B, S11, S12, Table S4**). To note that the fully dehydrated phase (no water hydrogen-bond interactions) exhibits only minor alterations compared to the fully hydrated structure (**Figure 3, S12, S15**).

To elucidate the templating effect of water H-bond network on the structural breathing, Density Functional Theory (DFT) calculations with periodic boundary conditions (PBC) were performed using the CRYSTAL17 suite software package.[26–28] Geometry optimizations of the fully hydrated iron and aluminum MOFs, using single crystal XRD data, were performed, resulting in perfectly hexagonal structures (**Figures S14, Table S5**). This led to minimal modifications (a slight relaxation of cell parameters <1.5%) while maintaining the H-bond network intact, confirming the robustness of the theoretical method and supporting the placement of hydrogen atoms, as such H-bond networks are prone to collapse. To avoid spin-related challenges and because the two MOFs are isostructural, subsequent calculations were carried out based the Al- phase. The simulations revealed that even a small amount of water induces significant scaffold distortions, as illustrated by series conversion H_{12}-Al_2-(DOBDP)$_3$·H_2O ↔ H_{12}-Al_2-(DOBDP)$_3$·2H_2O ↔ H_{12}-Al_2-(DOBDP)$_3$·4H_2O (**Figures S16-S19** and **Table S6**).

For the first two compositions, the water molecules are located in between the linkers, leading to topologies that deviate from the perfect hexagonal framework, positioned between those of H_{12}-Fe_2-(DOBDP)$_3$_d and H_{12}-Fe_2-(DOBDP)$_3$_ph (**Figure 3)**. Moving to H_{12}-Al_2-(DOBDP)$_3$.4H_2O, the water molecules reorganize and are found located into the pores, yielding an isostructural to the H_{12}-Fe_2-(DOBDP)$_3$_pd phase (rectangular, **Figure 3**). The simulated structure features an intra-pore hydrogen bond network linking opposite-facing O_2P-OH and phenolate -OH groups, pulling on the pore walls (**Figure S19**). The simulations emphasize the structural flexibility of these MOFs, driven by a hydrogen bonding network induced by water, which enables distortion even at minimal water content while preserving its structural integrity and

aligning closely with experimental extrapolations from XRD data (refer to the DFT section in the supplementary information for further details).

Given by the water accessibility in the pores, we performed water adsorption isotherm measurements on both Fe- and Al- MOFs (**Figure S20**). Both systems displayed type-IV adsorption isotherms, with H_{12}-Al_2-$(DOBDP)_3$ exhibiting a significant water uptake at relative pressure (P/P0) below 0.55, consistent with its higher BET surface area of 586 m^2/g compared to 403 m^2/g for H_{12}-Fe_2-$(DOBDP)_3$ (details in the supporting information). This suggests that the dehydrated phase of H_{12}-Al_2-$(DOBDP)_3$ MOF may possess higher hydrophilicity, periodicity, and rigidity compared to its Fe analogue. At a relative pressure (P/P0) of 1.0, the water content in Al and Fe phases was measured at 365 and 295 cm^3/g, respectively. This corresponds to 14 and 12 mols of water per mol of Al and Fe MOFs, indicating only two additional water molecules per formula unit in the Al-MOF compared to the Fe-MOF [H_{12}-Al_2-$(DOBDP)_3 \cdot 14H_2O$ vs. H_{12}-Fe_2-$(DOBDP)_3 \cdot 12H_2O$]. The higher water uptake of the Al-MOF compared to the Fe-MOF is attributed to differences in framework properties and interactions despite the structural similarity. The Al-MOF exhibits more pronounced structural breathing, while the Fe-MOF undergoes an additional intermediate structural phase change (_pd, **Figure 3**), which may limit the water uptake. Additionally, the Al(III)-oxygen bonds generating a more hydrophilic environment, enhancing water adsorption. Studies on isostructural materials such as Ga-MIL-53 and Al-MIL-53 have similarly attributed differences in water adsorption to coordination chemistry, molecular orbital considerations, and the presence of an intermediate structural phase in Ga-MIL-53.[20] These findings highlight the role of framework flexibility and interactions with water molecules in governing the adsorption properties of MOFs.

Mixed proton - electron transport in H_{12}-$(Fe/Al)_2$-$(DOBDP)_3$ MOFs

Examples of mixed-conducting MOFs remain scarce to date[11–14]with thus possibilities underexplored. To investigate the mixed conductivity of H_{12}-M_2-$(DOBDP)_3$ MOF (M = Fe, Al), we used Potentiostatic Electrochemical Impedance Spectroscopy (PEIS) and I-V measurements in a the two-probe configuration on pressed powder pellets (**Figure 4A**, **S22**, **S23**). Notably, H_{12}-Fe_2-$(DOBDP)_3$_h and H_{12}-Fe_2-$(DOBDP)_3$_ph phases were found to exhibit two distinct semi-circles in the measured PEIS profile (**Figure 4A**). These features indicate the presence of two resistance components, underscoring mixed protonic-electronic conductivity (refer to the experimental section for further details). By extrapolating the intercepts of both semi-circles with the x-axis, denoted as R_{LF} and R_{HF}, the relevant conductivity values were extracted using the Huggins method[29]. The R_{LF} intercept, corresponding to the low frequency semi-circle, yielded resistance values comparable to I-V measurements, attributed to electron transport (R_e); whereas R_{HF} accounts for mixed protonic and electronic conductivity contribution (refer to Experimental Procedures section).

At 293 K and 31% RH humidity, the proton and electrical conductivity of H_{12}-Fe_2-$(DOBDP)_3$_h were estimated at 1.6×10^{-4} and 8.7×10^{-7} $S.cm^{-1}$, respectively, which are orders of magnitude higher when compared to H_{12}-Fe_2-$(DOBDP)_3$_ph phase (**Figure 4** and **Table 2**). The reduction in proton conductivity upon dehydration is consistent with the typical role of solvation in facilitating proton transport. However, the decrease in electron conductivity is likely due to partial distortion of the secondary building units (SBUs) upon water removal, which hinders the electron hopping within the framework. The hydrated phases of H_{12}-M_2-$(DOBDP)_3$_h [M = Fe, Al, Sc, In] all were found to display comparable proton conductivities of 1.6×10^{-4} S cm^{-1}, 6.1×10^{-5} S cm^{-1}, 2.1×10^{-4} S cm^{-1}, and 1.7×10^{-1} S cm^{-1}, respectively. However, only the

tetrametallic MOF, similar to the Fe-based phase, demonstrated mixed proton (1.3 × 10^{-4} S cm^{-1}) and electronic (2.8 × 10^{-7} S cm^{-1}) conductivity (**Figure S24, Table S7**). Conversely, H_{12}-Al_2-(DOBDP)$_3$_ph displayed higher proton conductivity of 8.4 × 10^{-6} S cm^{-1}, as compared to H_{12}-Fe_2-(DOBDP)$_3$_ph (4.5 × 10^{-7} S cm^{-1}; **Figure 4** and **Table 2**), attributed to the higher water content in Al_ph ($8H_2O$) than in Fe_ph ($7H_2O$) (**Table 1**). While both, _h and _pd Fe-phases were found to display mixed proton and electron conductivity (**Figures 4**, **S22**), the equivalent Al-phases were found to be only proton conducting (**Figure S23**). The other dehydrated phases were found to be only poor electronic conductors (**Figure 4B**, **S22**, **S23** and **Table 2**).

The electron conductivity in the H_{12}-Fe_2-(DOBDP)$_3$ MOF is likely facilitated by a hopping mechanism involving Fe(III) redox centers, where the $[Fe(O_2P\text{-}OH)_3]_n$ one-dimensional chains, aligned along the *c*-axis (**Figure 4D**), serve as a pathway for charge transfer between Fe(III) sites.[9] In contrast, the Al-based MOF, characterized by redox-innocent $3s^0$ Al^{3+} centers, does not exhibit a similar electronic conductivity. The difference in electronic structure between the redox-active $3d^5$ Fe^{3+} and redox-innocent Al^{3+} appears responsible for this distinction. DFT calculations suggest that the lower band gap observed in Fe-MOF relative to Al-MOF supports the possibility of electronic conductivity in the Fe-based framework (Refer the DFT section in the Supporting Information for details).

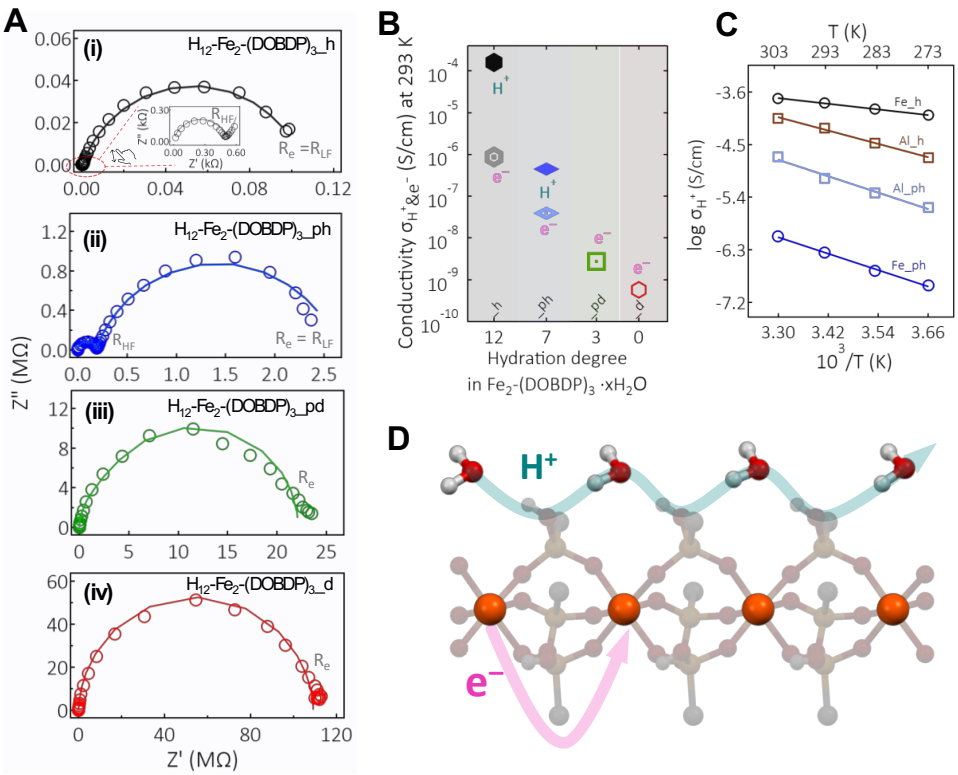

Figure 4. Proton-electron conductivity of H_{12}-M_2-(DOBDP)$_3$ [M= Fe, Al]

(A) Nyquist plots of the ac PEIS data profiles for the Fe-MOF at various hydration states.

(B) Estimated mixed conductivity function of water content for H_{12}-Fe_2-(DOBDP)$_3$ xH_2O phases, at 293K and 31% RH.

(C) Variable temperature proton conductivity for MPEC Fe/Al- _h and _ph phases.

(D) Plausible pathways for proton and electron (e^-) conductivity in H_{12}-Fe_2-(DOBDP)$_3$ MOF.

The activation energy (E_a) for proton transport in the Fe/Al- _h and _ph phases was determined by measuring the conductivity at various temperatures (**Figure 4C**, **S22**, and **S23**). The values align with previous reports for phosphonate-based MOFs (**Table S7**),[14,30–41] with the higher activation energies observed for _ph phases due to the reduced solvating water content, which limits proton mobility within the framework. This observation suggests a transition in the proton conduction mechanism from the Grotthuss mechanism (typically E_a < 0.4 eV) to the vehicle mechanism (typically E_a > 0.4 eV) or a combination of both mechanisms (**Figure 2B**).[8,42–44] Proton conductivity is facilitated by the P-OH groups in the presence of water, while electron transport is proposed to occur through redox hopping between Fe(III) centers along the $[Fe(O_2P\text{-}OH)_3]_n$ one-dimensional chains.

The role of water molecules is critical in the hydrated phases, where these facilitate the formation of a densely interconnected hydrogen-bond network (**Figure 2A**, **S4**), enhancing proton hopping (**Figure 2B, 4D**). Considering the pKa values of the protons in the H_4-$DOBDP^{2-}$ moiety of the MOF (pKa ~ 7 for P-OH and pKa ~ 15 for the phenolic O-H), it is more reasonable to assume that the proton conductivity arises primarily from the P-OH group in the presence of water. The crystal structure analysis also supports this, as the phenolates are not involved in the hydrogen-bond network channels (**Figure S4C**), underscoring the proton conductivity is mainly facilitated by uncoordinated phosphonate (**Figure 2B, 4D**). Thus, the weakly acidic protons involved in proton transport emphasize the significance of the dense hydrogen-bond framework in influencing the conductivity properties of these materials.

Table 2. Proton and electron conductivity of H_{12}-M_2-$(DOBDP)_3$ (M = Fe, Al) phases at 293K

	Conductivity, S/cm		
	Proton (from PEIS)	Electrical (from PEIS)	Electrical (from I-V)
H_{12}-Fe_2-$(DOBDP)_3$_h	1.6 **X** 10^{-04}	8.7 **X** 10^{-07}	8.3 **X** 10^{-07}
H_{12}-Fe_2-$(DOBDP)_3$_ph	4.5 **X** 10^{-07}	3.9 **X** 10^{-08}	3.4 **X** 10^{-08}
H_{12}-Fe_2-$(DOBDP)_3$_pd	-------	2.7 **X** 10^{-09}	2.6 **X** 10^{-09}
H_{12}-Fe_2-$(DOBDP)_3$_d	-------	5.7 **X** 10^{-10}	6.4 **X** 10^{-10}
H_{12}-Al_2-$(DOBDP)_3$_h	6.1 **X** 10^{-05}	-------	-------
H_{12}-Al_2-$(DOBDP)_3$_ph	8.4 **X** 10^{-06}	-------	-------
H_{12}-Al_2-$(DOBDP)_3$_d	-------	2.1 **X** 10^{-10}	1.7 **X** 10^{-10}

Reversible Redox Behavior of H_{12}-M_2-$(DOBDP)_3$ [Fe, Al] MOFs

To confirm the redox behavior of H_{12}-M_2-$(DOBDP)_3$_h [Fe, Al] MOFs, enabled by the uncoordinated enolate functionalities,[22] chemical method oxidation - reduction, and solid-electrode cyclic voltammetry (CV) were employed (**Figure 5**). Upon chemical oxidation, the Al-MOF exhibited a pronounced color change from off-white to orange, while the Fe-MOF showed only a slight shift, transitioning from dark yellow (**Figure 5A**). FT-IR analysis revealed the appearance of a the C=O carbonyl band at 1659 cm^{-1} upon oxidation, and dissapearance after reduction in both Fe- and Al-based MOFs, with no significant band shifts, suggesting framework stability (**Figure 5B**, **Figure S25B**). Similarities in the diffractograms after oxidation, with notable changes in peak intensities, suggest that the structural integrity of the MOFs is largely maintained (**Figure S25C**). CV measurements further confirm the reversible redox

nature of the conjugated carbonyl center. The similarity in CV behavior for both MOFs suggests that the observed redox activity originates from the hydroquinone/quinone couple, rather than the Fe center. Three oxidation peaks were observed at 0.605 ± 0.005 V (O1, main), 0.44 V (O2), and 0.22 ± 0.01 V (O3), while corresponding reduction peaks were found at 0.55 ± 0.01 V (R1), 0.38 V (R2), and 0.195 ± 0.005 V (R3) for both MOFs (**Figure 5C**). These multiple redox peaks are characteristic of DOBDP systems in the solid state, as previously observed with Li_4-Zn-DOBDP.[15]

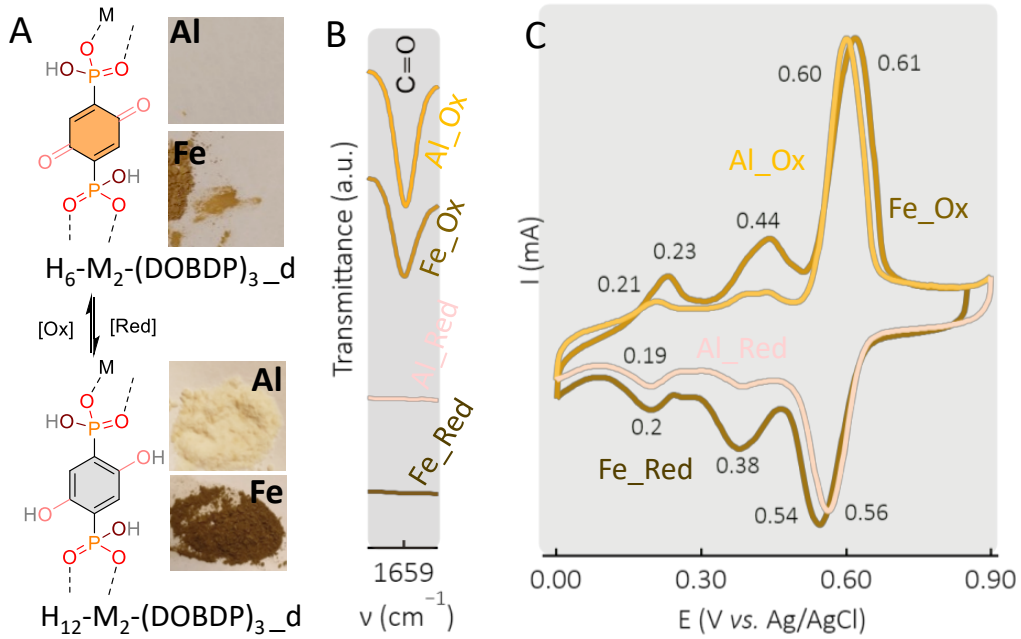

Figure 5. Chemical and electrochemical reversible redox behavior in H_{12}-M_2-(DOBDP)$_3$ [M=Fe, Al]

(A) Schematic of hydroquinone - quinone redox and corresponding color changes.
(B) FTIR evidence of the carbonyl band upon oxidation.
(C) CV displaying the reversible redox of thye DOBDP system[15].

CONCLUSIONS

A series of crystalline monometallic phosphonate-based 3D MOFs, denoted as H_{12}-Fe_2-(DOBDP)$_3$ [M = Fe, Al, Sc, In], along with one tetrametallic analogue, are reported. These are constructed via phosphonate coordination (O=P-O....M), with each phosphonate group containing a free hydroxy group [(HO-(PO_2-M)] that enables proton transport in the presence of water and of a dense Hydrogen bonding network within the pores. The Fe and Al MOFs exhibit reversible breathing behavior, transitioning between fully hydrated and dehydrated states with four and respectively three distinct phases. The fully hydrated (_h) and partially hydrated (_ph) phases of the H_{12}-Fe_2-(DOBDP)$_3$ demonstrated mixed proton and electron conduction (MPEC), whereas H_{12}-Al_2-(DOBDP)$_3$ phases display only proton conductivity. The proton transport mechanism proceeds via a Grotthuss mechanism (Ea < 0.4 eV), vehicular mechanism (Ea > 0.4 eV), or a combination of both, depending on the water content. Electron transport occurs through a hopping process along the [Fe(O_2P-OH)$_3$]$_n$ one-dimensional chain. At 293 K and ambient conditions, the fully hydrated H_{12}-Fe_2-

$(DOBDP)_3$_h MOF exhibits proton and electrical conductivities of 1.6×10^{-4} and 8.7×10^{-7} S cm^{-1}, respectively. The reversible redox activity of the uncoordinated hydroquinone functionality in Al- and Fe-MOFs is confirmed through both chemical oxidation-reduction and electrochemical analysis. Overall, this study highlights the water-induced structural dynamics, proton-electron conductivity properties and redox behavior of H_{12}-M_2-$(DOBDP)_3$ [M= Al, Fe] MOFs, and paves the way for new multifunctional design strategies for materials at the intersection of chemistry, physics, and energy science.

EXPERIMENTAL PROCEDURES

Resource availability

Lead contact

Further information and requests for resources should be directed to and will be fulfilled by the lead contact, Alexandru VLAD (alexandru.vlad@uclouvain.be).

Materials availability

All materials generated in this study are available from the lead contact without restriction, and upon reasonable request.

Data and code availability

This study did not generate any datasets.

Materials (chemicals and reagents):

The following chemical were used without further purification: 2,5-Dihydroxy-1,4-benzenediphosphonic acid (H_6-DOBDP, 98%, Epsilon Chimie), Iron(II) perchlorate hydrate (Reagent Grade, Alfa Aesar), Iron(III) nitrate nonahydrate (98% metals basis, Alfa Aesar), Aluminium(III) nitrate nonahydrate (ACS reagent, 98%, Sigma Aldrich), Indium(III) nitrate hydrate (99.99 % metals basis, Alfa Aesar) and Scandium(III) trifluoromethanesulfonate (99%, Fluorochem), Conc. HCl (37% , VWR), Conc. H_2SO_4 (98%, VWR), $NOBF_4$ (95%, Sigma Aldrich), Acetonitrile, Methanol (99.8%, anhydrous, Thermo Scientific), Ethanol (absolute, VWR), Sodium cyanoborohydride ($NaBH_3CN$, 95%, Thermo Scientific), and Polytetrafluoroethylene (PTFE, from Sigma Aldrich).

Instrumentation:

Fourier transform Infra-Red (FTIR) spectroscopy was carried out using Agilent Technologies Cary 630 FTIR spectrometer operated in transmission or ATR mode. Thermogravimetric analysis (TGA) was carried out under argon with a SENSY Sevo instrument (Setaram) at a heating rate of 10 °C/min, between 25 and 900°C, under nitrogen atmosphere. Water sorption measurements at 298 K were performed on AQUA3-Belsorp Solvent Adsorption instrument. Samples were first degassed at 150 °C and 1×10^{-1} Pa vacuum for 12 h for Al-MOF and at 90 °C and 1×10^{-1} Pa vacuum for 2 h for Fe-MOF before performing sorption isotherm measurement. X-ray powder diffraction (XRD) patterns were collected on STOE DARMSTADT Transmission diffractometer system using Mo K**α**1 radiation with a wavelength of 0.70930 Å. In situ XRD data (heating, dehydration) was collected using a MAR345 image-plate detector equipped with an Incoatec Mo (**λ** = 0.71073 Å) Microfocus (IμS 2.0) X-ray source operating at 50 kV and 1000 μA. The resulting two-dimensional images were azimuthally integrated using the Fit2D software, with LaB_6 serving as a calibrant. The samples were loaded into 0.7 mm glass capillaries (Hilgenberg GmbH); vacuum and heating were applied through a home-built gas dosing system equipped with an oil-pump and a Leister LE MINI SENSOR KIT hot air blower (Leister Technologies Benelux B.V.). SEM images were acquired on Zeiss Neon 40 crossbeam

workstation with Gemini SEM column (Carl Zeiss Iberia, S.L, Madrid, Spain). Elemental analysis (CHNS) was done with Thermo Scientific™ FlashSmart™ Elemental Analyzer. Inductively coupled plasma-optical emission spectrometry (ICP-OES) analysis was performed on Perkin Elmer™ Avio220 max.

Single crystal X-ray data collection on H_{12}-Al/Fe_2-$(DOBDP)_3 \cdot 21H_2O$ (_sh) was carried out on MAR345 image plate detector using Mo-K**α** radiation (0.71073 Å) generated by a Rigaku UltraX18S rotating anode (Xenocs Fox3D mirror). Prior to measurement, the crystal was flash cooled to 150 K in a N_2 gaseous stream. Data acquisition, reduction and analytical face-index based absorption correction were made using CrysAlisPRO[45] software, and the implemented absorption correction was applied. The structure was solved by SHELXT and refined by SHELXL2014/7.[46] All non-hydrogen atoms were refined anisotropically and H atoms were placed on calculated positions and refined in riding mode on their parent atoms with isotropic temperature factors, fixed at 1.2Ueq of the parent atoms. The crystal and refinement data are summarized in Table S1.

CCDC numbers 2395265 (for H_{12}-Fe_2-$(DOBDP)_3 \cdot 21H_2O$) and 2395266 (for H_{12}-Al_2-$(DOBDP)_3 \cdot 9H_2O$+5.5O+solvent) contains the supplementary crystallographic data, available free of charge from The Cambridge Crystallographic Data Centre via www.ccdc.cam.ac.uk/structures

Mixed conductivity measurement and analysis:

Pellets with a diameter of 7 mm were prepared by placing 40 mg of powder into custom designed Swagelok cells. The powder was cold pressed at an applied pressure of 2 T, between two carbon coated Aluminum foils to ensure a good contact and the cell locked to maintain the pressure. Variable temperature conductivity measurements were conducted in a climatic chamber, with continuous applied pressure. A Bio-Logic potentiostat was employed for the conductivity measurements, which included Potentiostatic Electrochemical Impedance Spectroscopy (PEIS) across a frequency range from 7 MHz to 10 mHz with a 200 mV amplitude ac signal. Electrical conductivity was measured using I-V dc measurements with either the Bio-Logic or a Keithley 2400 source meter, both in a two-probe configuration.

The mixed conductivity analysis was performed according to Huggins method[29], and electrical conductivity confirmed by dc I-V measurements. For a material exhibiting substantial (or comparable) ion (proton) and electronic transport, the PEIS can reveal two semicircles. According to method used, the first semicircle corresponds to ion (proton) transport component, while the second semicircle relates to electron transport. The low frequencies intercept (R_{LF}) consistently resulted in similar to the measured dc I-V values, and relates to the electronic resistance - $R_e = R_{LF}$. The high frequency intercept, R_{HF}, is a combination of the two resistances, R_p and R_e (p=proton e=electronic), according to the Equation 1:

$$1/R_{HF} = 1/R_p + 1/R_e \quad \text{(eq. 1)}$$

the ionic and electronic contribution to the total conductance, and thus of the conductivity, can be estimated using the following equations:

- Proton conductance, $G_p = 1/R_p = 1/R_{HF} - 1/R_e = (R_e - R_{HF})/(R_{HF}R_e)$;
- Electronic conductance, $G_e = 1/R_e = 1/R_{LF}$;
- Proton/ electronic conductivity, $\sigma_{p/e} = G_{p/e}(L/A)$ [L = thickness, A = area].

Computational (DFT) details:

To rationalize the structure of the intermediate de/hydrated phases of the Al and Fe MOFs, Periodic Boundary Condition (PBC) Density Functional Theory (DFT) calculations were conducted using the CRYSTAL17 package.[26,27] The calculations involved full geometry optimization, in which both the atomic coordinates and cell parameters were relaxed while maintaining the chosen space group symmetry. Geometry optimizations utilized the **ω**B97X exchange-correlation functional (XCF)[47] and the valence triple zeta basis set with polarization function, specifically the POB_TZVP_rev2 basis set.[48] PBC-related parameters included: i) thresholds for truncation of lattice summations over the integrals (TOLINTEG 11 11 11 40 90), and ii) first Brillouin zone sampling (SHRINK 8 24). The choice of XCF and basis set was based on prior studies.[28]

Before optimizing the iron-based MOFs, additional calculations were performed to assess the spin multiplicity of the iron centers. An iron atom and its surrounding environment were extracted from the crystal structure, with dangling bonds saturated by hydrogen atoms (see Figure S13). This geometry was kept frozen during subsequent single-point calculations conducted with the GAUSSIAN16 package.[49] Spin multiplicities of doublet, quadruplet, and sextuplet states were imposed, employing the **ω**B97X-D functional[50] and the 6-311+G** basis set (See www.basissetexchange.org for EMSL/PNNL Basis set Exchange).

Cyclic voltammetry (CV):

Solid-electrode cyclic voltammetry (CV) was performed using a Bio-Logic instrument with a three-electrode setup. The working electrode was prepared by grinding H_{12}-M_2-(DOBDP)$_3$_h [Fe, Al] MOF, SP carbon, and PTFE binder (60:30:10). The resulting composite was dispersed in ethanol and drop-cast onto a glassy carbon (GC) electrode. The reference electrode (RE) was Ag/AgCl in saturated KCl, and the counter electrode (CE) was graphite. The electrolyte used was 1 M H_2SO_4. CV measurements were recorded with a scan rate of 10 mV/s, within the potential range of 0.9V to 0V vs Ag/AgCl for Al-MOF and 0.85V to 0.0V for Fe-MOF.

Synthetic procedures:

Synthesis of H_{12}-Fe_2-(DOBDP)$_3$ ·21H_2O (_sh) (Single crystal, mixed phase): Typically, H_6-DOBDP (0.2 mmol) was placed in a 20 mL glass vial and dissolved with 2 mL deionized water. In parallel, $Fe(ClO_4)_2$·xH_2O (0.2 mmol, calculated on anhydrous basis), was dissolved in 1 ml deionized water. This Fe(II)-salt solution was then added dropwise to the H_6-DOBDP solution. The resulting clear solution was caped and placed in an oven at 70°C for 48 hours. The yellow product comprising single hexagonal crystals and powder was filtered, washed with deionized water (5 mL × 3), and left to dry in ambient air. Single crystals were manually separated from reaction mixture and used for Single crystal XRD. The purity of the bulk powder was verified by powder XRD, which indicated a phase impurity (**Figure S1**). To obtain a pure phase, different protocol was developed as described in the following.

Synthesis of H_{12}-Fe_2-(DOBDP)$_3$_h (bulk crystalline powder, pure phase): Typically, H_6-DOBDP (0.3 mmol) was placed in a 20 mL glass vial and dissolved in 2 mL of deionized water, to which 200 µL of concentrated HCl was added. In parallel, $Fe(NO_3)_3$ ·9H_2O (0.2 mmol) was dissolved in 1 mL of deionized water, and the Fe(III) salt solution was added dropwise to the H_6-DOBDP solution. A gel-like dark red/black precipitate formed immediately. The vial was capped and kept in an oven at 40°C for 72 hours without disturbance. The dark yellow solid product was then separated by filtration, washed with deionized water (5 mL, 3 times), and dried in open ambient air (yield: 81 mg, 72% based on H_{12}-Fe_2-(DOBDP)$_3$·12H_2O). Powder XRD data confirmed the phase

purity (see **Figure S1**). The powder form of pristine H_{12}-Fe_2-$(DOBDP)_3 \cdot 12H_2O$ was used for further studies.

Syntheses of H_{12}-Al_2-$(DOBDP)_3 \cdot 21H_2O$ (_sh) (single crystals): Typically, H_6-DOBDP (0.3 mmol) and $Al(NO_3)_3 \cdot 9H_2O$ (0.2 mmol) were placed in a 20 mL glass vial and dissolved in 3 mL of deionized water. The vial was capped and kept at room temperature for two years, during which suitable crystals grew for single crystal XRD.

Syntheses of H_{12}-Al_2-$(DOBDP)_3$_h (powder form, room temperature and 40°C): Typically, H_6-DOBDP (0.3 mmol) and $Al(NO_3)_3 \cdot 9H_2O$ (0.2 mmol) were placed in a 20 mL glass vial and dissolved in 3 mL of deionized water. The vial was capped and kept at room temperature for one month (crystal nucleation observed within one week); or at 40°C for 14 days. Off-white crystalline powder was separated by filtration, washed with deionized water (5 mL, 3 times), and dried in open ambient air (yield: 31 mg for RT, 29% based on H_{12}-Al_2-$(DOBDP)_3 \cdot 12H_2O$); 72 mg for 40°C, 67% based on H_{12}-Al_2-$(DOBDP)_3 \cdot 12H_2O$). The obtained products from the H_{12}-Al_2-$(DOBDP)_3$ synthesis at RT and 40°C exhibited similar powder XRD patterns (**Figure S2**), confirming the formation of the same product. The powder form obtained at 40°C was selected for further studies.

Syntheses of H_{12}-Sc_2-$(DOBDP)_3$_h: Typically, H_6-DOBDP (0.3 mmol) was placed in a 20 mL glass vial and dissolved in 2 mL of deionized water. In parallel, $Sc(CF_3SO_3)_3$ (0.2 mmol) was dissolved in 1 mL of deionized water. The Sc(III) salt solution was added dropwise to the H_6-DOBDP solution, resulting in the formation of a white gel precipitate. The vial was capped and kept in an oven at 40°C for 5 days without disturbance. The white solid product was filtered, washed with deionized water (5 mL, 3 times), and dried in open ambient air (yield: 87 mg, 67% based on H_{12}-Sc_2-$(DOBDP)_3 \cdot 18H_2O$).

Syntheses of H_{12}-In_2-$(DOBDP)_3$_h: Typically, H_6-DOBDP (0.3 mmol) was placed in a 20 mL glass vial and dissolved in 2 mL of deionized water. In parallel, $In(NO_3)_2 \cdot xH_2O$ (0.2 mmol, calculated on anhydrous basis) was dissolved in 1 mL of deionized water, and was added dropwise to the H_6-DOBDP solution. A white gel precipitate formed immediately. The vial was capped and kept in an oven at 40°C for 5 days without disturbance. The white solid product was filtered, washed with deionized water (5 , 3 rimes), and dried in open ambient air (yield: 76 mg, 56% based on H_{12}-In_2-$(DOBDP)_3 \cdot 18H_2O$).

Syntheses of tetra metallic MOF H_{12}-(Fe,Al,Sc,In)$_2$-$(DOBDP)_3$: The same protocol as for the synthesis of "H_{12}-Fe_2-$(DOBDP)_3$_h bulk crystalline powder" was adopted, with a quaternary mixture of 0.025 mmol of each metal precursor used. The ratio of Fe:Al:Sc:In (0.62:0.12:0.88:0.38) were determined by inductively coupled plasma-optical emission spectrometry (ICP-OES).

Dehydration of H_{12}-M_2-$(DOBDP)_3$_h MOFs: Partially hydrated (_ph) samples were obtained by applying vacuum at room temperature for 10 hours. Partially dehydrated Fe(III) (_pd) samples were prepared under vacuum in inert conditions. Complete dehydration was achieved by heating pristine or partially desolvated phases in a Büchi glass oven under vacuum (inside an Ar-filled glovebox) at 150°C for 5 hours.

Re-hydration of partial hydrated (_ph) partial dehydrated (_pd) and dehydrated (_d) MOFs (RT, 150°C **vacuum dried MOFs):** Water was added to both partially and completely dehydrated MOF samples. For Fe(III), Al(III), and Sc(III) MOFs, partially

(de)hydrated (_ph/_pd) samples were kept under ambient conditions for 1 hour, while for In(III), they were maintained at 40°C for 72 hours. For completely dehydrated (_d) samples, Fe(III) and Al(III) MOFs were rehydrated under ambient conditions for 1 hour, whereas Sc(III) and In(III) MOFs were kept at 70°C for 7 days. Excess water was removed by filtration, and the rehydrated phases were analyzed by XRD.

Chemical Oxidation-Reduction of H_{12}-M_2-$(DOBDP)_3$ [M = Fe, Al]: The reactions were carried out in an argon-filled glovebox. H_{12}-M_2-$(DOBDP)_3$_d (M = Al, Fe; 0.04 mmol) was suspended in 5 mL of acetonitrile in a 20 mL glass vial, followed by the addition of $NOBF_4$ (0.26 mmol, 6.5 eq) in 5 mL of acetonitrile. The vial was loosely capped to allow NO gas evolution. The mixture was stirred at room temperature for 36 hours. The resulting oxidized MOF suspensions (orange for Al; dark yellow, with no significant color change for Fe) were centrifuged, washed with acetonitrile (3 × 5 mL), and dried under vacuum at room temperature. Reduction of the oxidized phases followed the same procedure as oxidation, differing only in the choice of reducing agents, solvent composition, and drying conditions, e.g. sodium cyanoborohydride ($NaBH_3CN$, 6.5 eq, in methanol) was used, followed by drying at 150°C under vacuum.

SUPPLEMENTAL INFORMATION

This section should include the titles and (optional) legends of all supplemental items. Document S1 is the main supplemental PDF:

ACKNOWLEDGMENTS

The major core of the work was funded through FWO and F.R.S.-FNRS under the Excellence of Science program (EOS 40007515). Partial support was received from the European Research Council under the European Union's Horizon 2020 research and innovation program (grant agreement No. 770870, MOOiRE – A.V.) as well as F.R.S.-FNRS through F.4552.21-P grant. D.R. B.V.R, and X.L acknowledge F.R.S.-FNRS for Chargé de Recherché (CR) fellowship (grant agreement No. 40010410, 40023657 and 40010559). T.G. R.M. and G.C. acknowledges F.R.S.-FNRS for PhD fellowships. D.T. X.G. and Y.Z. acknowledge CSC for the PhD fellowships. D.R. thanks Dr. Marshal Maskarenj for helpful discussions.

AUTHOR CONTRIBUTIONS

D.R. and A.V. conceived and designed the project. D.R. and T.G., have contributed performed the major part of the experimental work, assisted by V.R.B., P.A., T.S., S.K., X.G., S.P., A.R., Y.Z. F.M., P.B., and B.C. performed DFT calculations. D.R. and K.R. performed the crystal structure analysis. S.P., R.M., G.C., X.L., P.X., involved in SEM and TEM analysis. S.K. and T.K.M., involved water adsorption studies. T.S. and Y.F., involved in in situ XRD analysis. D.R. performed conductivity measurements, assisted by V.R.B., S.P., T.G., P.A., D.T. D.R., A.R., V.F., and T.G. involve in redox behavior analysis. All authors made iterative contributions and changes to the experiments during implementation and subsequent analysis, working collaboratively as a team. All authors contributed to the scientific discussion of the results as well as participated in the writing and approved the manuscript.

DECLARATION OF INTERESTS

The authors declare no competing interests.

REFERENCES

1. Strietzel, C., Sterby, M., Huang, H., Strømme, M., Emanuelsson, R., and Sjödin, M. (2020). An Aqueous Conducting Redox-Polymer-Based Proton Battery that Can Withstand Rapid Constant-Voltage Charging and Sub-Zero Temperatures. Angew. Chemie Int. Ed. *59*, 9631–9638. 10.1002/anie.202001191.
2. Song, Y., Chen, Y., Wang, W., Zhou, C., Zhong, Y., Yang, G., Zhou, W., Liu, M., and Shao, Z. (2019). Self-Assembled Triple-Conducting Nanocomposite as a Superior Protonic Ceramic Fuel Cell Cathode. Joule *3*, 2842–2853. 10.1016/j.joule.2019.07.004.
3. Zhu, Y., He, Z., Choi, Y., Chen, H., Li, X., Zhao, B., Yu, Y., Zhang, H., Stoerzinger, K.A., Feng, Z., et al. (2020). Tuning proton-coupled electron transfer by crystal orientation for efficient water oxidization on double perovskite oxides. Nat. Commun. *11*, 4299. 10.1038/s41467-020-17657-9.
4. Fabbri, E., Pergolesi, D., and Traversa, E. (2010). Materials challenges toward proton-conducting oxide fuel cells: a critical review. Chem. Soc. Rev. *39*, 4355. 10.1039/b902343g.
5. Cao, L., Wu, H., Mu, Z., He, X., Wang, C., Li, J., Li, Y., Xu, M., and Jiang, Z. (2018). Phosphorylated graphene monoliths with high mixed proton/electron conductivity. J. Mater. Chem. A *6*, 8499–8506. 10.1039/C8TA02500B.
6. Wind, J., Mole, R.A., Yu, D., Avdeev, M., and Ling, C.D. (2018). Hydration Mechanisms and Proton Conduction in the Mixed Ionic–Electronic Conductors Ba 4 Nb 2 O 9 and Ba 4 Ta 2 O 9. Chem. Mater. *30*, 4949–4958. 10.1021/acs.chemmater.8b00950.
7. Hatakeyama, K., Tateishi, H., Taniguchi, T., Koinuma, M., Kida, T., Hayami, S., Yokoi, H., and Matsumoto, Y. (2014). Tunable Graphene Oxide Proton/Electron Mixed Conductor that Functions at Room Temperature. Chem. Mater. *26*, 5598–5604. 10.1021/cm502098e.
8. Lim, D.-W., and Kitagawa, H. (2020). Proton Transport in Metal–Organic Frameworks. Chem. Rev. *120*, 8416–8467. 10.1021/acs.chemrev.9b00842.
9. Xie, L.S., Skorupskii, G., and Dincă, M. (2020). Electrically Conductive Metal–Organic Frameworks. Chem. Rev. *120*, 8536–8580. 10.1021/acs.chemrev.9b00766.
10. Apostol, P., Gali, S.M., Su, A., Tie, D., Zhang, Y., Pal, S., Lin, X., Bakuru, V.R., Rambabu, D., Beljonne, D., et al. (2023). Controlling Charge Transport in 2D Conductive MOFs—The Role of Nitrogen-Rich Ligands and Chemical Functionality. J. Am. Chem. Soc. 10.1021/jacs.3c07503.
11. Su, J., He, W., Li, X.-M., Sun, L., Wang, H.-Y., Lan, Y.-Q., Ding, M., and Zuo, J.-L. (2020). High Electrical Conductivity in a 2D MOF with Intrinsic Superprotonic Conduction and Interfacial Pseudo-capacitance. Matter *2*, 711–722. 10.1016/j.matt.2019.12.018.
12. Choi, J.Y., Stodolka, M., Kim, N., Pham, H.T.B., Check, B., and Park, J. (2022). 2D conjugated metal-organic framework as a proton-electron dual conductor. Chem, 1–11. 10.1016/j.chempr.2022.09.016.
13. Lu, C., Choi, J.Y., Check, B., Fang, X., Spotts, S., Nuñez, D., and Park, J. (2024). Thiatruxene-Based Conductive MOF: Harnessing Sulfur Chemistry for Enhanced Proton Transport. J. Am. Chem. Soc. *146*, 26313–26319. 10.1021/jacs.4c08659.
14. Ribeiro, C., Tan, B., Figueira, F., Mendes, R.F., Calbo, J., Valente, G., Escamilla, P., Paz, F.A.A., Rocha, J., Dincă, M., et al. (2025). Mixed Ionic and Electronic Conductivity in a Tetrathiafulvalene-Phosphonate Metal–Organic Framework. J. Am. Chem. Soc. *147*, 63–68. 10.1021/jacs.4c13792.
15. Zhang, Y., Wang, J., Apostol, P., Rambabu, D., Eddine Lakraychi, A., Guo, X., Zhang, X., Lin, X., Pal,

S., Rao Bakuru, V., et al. (2023). Bimetallic Anionic Organic Frameworks with Solid-State Cation Conduction for Charge Storage Applications. Angew. Chemie Int. Ed. *62*. 10.1002/anie.202310033.

16. Ji, Z., Li, T., and Yaghi, O.M. (2020). Sequencing of metals in multivariate metal-organic frameworks. Science (80-.). *369*, 674–680. 10.1126/science.aaz4304.

17. Millange, F., Guillou, N., Walton, R.I., Grenèche, J.M., Margiolaki, I., and Férey, G. (2008). Effect of the nature of the metal on the breathing steps in MOFs with dynamic frameworks. Chem. Commun., 4732–4734. 10.1039/b809419e.

18. Henke, S., Schneemann, A., Wütscher, A., and Fischer, R.A. (2012). Directing the Breathing Behavior of Pillared-Layered Metal–Organic Frameworks via a Systematic Library of Functionalized Linkers Bearing Flexible Substituents. J. Am. Chem. Soc. *134*, 9464–9474. 10.1021/ja302991b.

19. Murdock, C.R., Hughes, B.C., Lu, Z., and Jenkins, D.M. (2014). Approaches for synthesizing breathing MOFs by exploiting dimensional rigidity. Coord. Chem. Rev. *258–259*, 119–136. 10.1016/j.ccr.2013.09.006.

20. Coudert, F.-X., Ortiz, A.U., Haigis, V., Bousquet, D., Fuchs, A.H., Ballandras, A., Weber, G., Bezverkhyy, I., Geoffroy, N., Bellat, J.-P., et al. (2014). Water Adsorption in Flexible Gallium-Based MIL-53 Metal–Organic Framework. J. Phys. Chem. C *118*, 5397–5405. 10.1021/jp412433a.

21. Alhamami, M., Doan, H., and Cheng, C.-H. (2014). A Review on Breathing Behaviors of Metal-Organic-Frameworks (MOFs) for Gas Adsorption. Materials (Basel). *7*, 3198–3250. 10.3390/ma7043198.

22. Rambabu, D., Lakraychi, A.E., Wang, J., Sieuw, L., Gupta, D., Apostol, P., Chanteux, G., Goossens, T., Robeyns, K., and Vlad, A. (2021). An Electrically Conducting Li-Ion Metal–Organic Framework. J. Am. Chem. Soc. *143*, 11641–11650. 10.1021/jacs.1c04591.

23. Shannon, R.D. (1976). Revised effective ionic radii and systematic studies of interatomic distances in halides and chalcogenides. Acta Crystallogr. Sect. A *32*, 751–767. 10.1107/S0567739476001551.

24. Zorainy, M.Y., Gar Alalm, M., Kaliaguine, S., and Boffito, D.C. (2021). Revisiting the MIL-101 metal–organic framework: design, synthesis, modifications, advances, and recent applications. J. Mater. Chem. A *9*, 22159–22217. 10.1039/D1TA06238G.

25. Steenhaut, T., Hermans, S., and Filinchuk, Y. (2020). Green synthesis of a large series of bimetallic MIL-100(Fe,M) MOFs. New J. Chem. *44*, 3847–3855. 10.1039/D0NJ00257G.

26. Dovesi, R., Erba, A., Orlando, R., Zicovich-Wilson, C.M., Civalleri, B., Maschio, L., Rérat, M., Casassa, S., Baima, J., Salustro, S., et al. (2018). Quantum-mechanical condensed matter simulations with CRYSTAL. WIREs Comput. Mol. Sci. *8*. 10.1002/wcms.1360.

27. Dovesi, R., Pascale, F., Civalleri, B., Doll, K., Harrison, N.M., Bush, I., D'Arco, P., Noël, Y., Rérat, M., Carbonnière, P., et al. (2020). The CRYSTAL code, 1976–2020 and beyond, a long story. J. Chem. Phys. *152*. 10.1063/5.0004892.

28. Mairesse, F., and Champagne, B. (2024). Simple scaling of the empirical London dispersion corrections in DFT geometry optimizations of prototypical nonlinear optical crystals. Int. J. Quantum Chem. *124*. 10.1002/qua.27275.

29. Huggins, R.A. (2002). Simple method to determine electronic conductivity and ionic components of the conductors in mixed a review. Ionics (Kiel). *8*, 300–313. 10.1007/BF02376083.

30. Taylor, J.M., Mah, R.K., Moudrakovski, I.L., Ratcliffe, C.I., Vaidhyanathan, R., and Shimizu, G.K.H. (2010). Facile Proton Conduction via Ordered Water Molecules in a Phosphonate Metal−Organic Framework. J. Am. Chem. Soc. *132*, 14055–14057. 10.1021/ja107035w.

31. Kim, S., Dawson, K.W., Gelfand, B.S., Taylor, J.M., and Shimizu, G.K.H. (2013). Enhancing Proton Conduction in a Metal–Organic Framework by Isomorphous Ligand Replacement. J. Am. Chem. Soc. *135*, 963–966. 10.1021/ja310675x.

32. Ramaswamy, P., Wong, N.E., Gelfand, B.S., and Shimizu, G.K.H. (2015). A Water Stable Magnesium MOF That Conducts Protons over 10 –2 S cm – 1. J. Am. Chem. Soc. *137*, 7640–7643. 10.1021/jacs.5b04399.

33. Firmino, A.D.G., Mendes, R.F., Antunes, M.M., Barbosa, P.C., Vilela, S.M.F., Valente, A.A., Figueiredo, F.M.L., Tomé, J.P.C., and Paz, F.A.A. (2017). Robust Multifunctional Yttrium-Based Metal–Organic Frameworks with Breathing Effect. Inorg. Chem. *56*, 1193–1208. 10.1021/acs.inorgchem.6b02199.

34. Rautenberg, M., Bhattacharya, B., Das, C., and Emmerling, F. (2022). Mechanochemical Synthesis of Phosphonate-Based Proton Conducting Metal–Organic Frameworks. Inorg. Chem. *61*, 10801–10809. 10.1021/acs.inorgchem.2c01023.

35. Rhauderwiek, T., Wolkersdörfer, K., Øien-Ødegaard, S., Lillerud, K.-P., Wark, M., and Stock, N. (2018). Crystalline and permanently porous porphyrin-based metal tetraphosphonates. Chem. Commun. *54*, 389–392. 10.1039/C7CC07766A.

36. Pili, S., Argent, S.P., Morris, C.G., Rought, P., García-Sakai, V., Silverwood, I.P., Easun, T.L., Li, M., Warren, M.R., Murray, C.A., et al. (2016). Proton Conduction in a Phosphonate-Based Metal–Organic Framework Mediated by Intrinsic "Free Diffusion inside a Sphere." J. Am. Chem. Soc. *138*, 6352–6355. 10.1021/jacs.6b02194.

37. Vilela, S.M.F., Navarro, J.A.R., Barbosa, P., Mendes, R.F., Pérez-Sánchez, G., Nowell, H., Ananias, D., Figueiredo, F., Gomes, J.R.B., Tomé, J.P.C., et al. (2021). Multifunctionality in an Ion-Exchanged Porous Metal-Organic Framework. J. Am. Chem. Soc. *143*, 1365–1376. 10.1021/jacs.0c10421.

38. Taylor, J.M., Dawson, K.W., and Shimizu, G.K.H. (2013). A Water-Stable Metal–Organic Framework with Highly Acidic Pores for Proton-Conducting Applications. J. Am. Chem. Soc. *135*, 1193–1196. 10.1021/ja310435e.

39. Wong, N.E., Ramaswamy, P., Lee, A.S., Gelfand, B.S., Bladek, K.J., Taylor, J.M., Spasyuk, D.M., and Shimizu, G.K.H. (2017). Tuning Intrinsic and Extrinsic Proton Conduction in Metal-Organic Frameworks by the Lanthanide Contraction. J. Am. Chem. Soc. *139*, 14676–14683. 10.1021/jacs.7b07987.

40. Zhou, Y.-N., Liu, L.-L., Liu, Q.-W., Liu, X.-X., Feng, M.-Z., Wang, L., Sun, Z.-G., Zhu, Y.-Y., Zhang, X., and Jiao, C.-Q. (2021). Dual-Functional Metal–Organic Framework for Luminescent Detection of Carcinoid Biomarkers and High Proton Conduction. Inorg. Chem. *60*, 17303–17314. 10.1021/acs.inorgchem.1c02655.

41. Huang, Y., Zhou, F., Feng, J., Zhao, H., Qi, C., Ji, J., Bao, S., and Zheng, T. (2021). An ultra-stable hafnium phosphonate MOF platform for comparing the proton conductivity of various guest molecules/ions. Chem. Commun. *57*, 1238–1241. 10.1039/D0CC07375J.

42. Canivet, J., Fateeva, A., Guo, Y., Coasne, B., and Farrusseng, D. (2014). Water adsorption in MOFs: fundamentals and applications. Chem. Soc. Rev. *43*, 5594–5617. 10.1039/C4CS00078A.

43. Kharod, R.A., Andrews, J.L., and Dincˇ, M. (2022). Teaching Metal-Organic Frameworks to Conduct: Ion and Electron Transport in Metal-Organic Frameworks. Annu. Rev. Mater. Res. 10.1146/annurev-matsci-080619.

44. Otake, K., and Kitagawa, H. (2021). Control of Proton-Conductive Behavior with Nanoenvironment within Metal–Organic Materials. Small *17*. 10.1002/smll.202006189.

45. CrysAlisPro, Version 1.171.37.35 (2014). at Agilent Technologies:Oxford.

46. Sheldrick, G.M. (2008). A short history of SHELX. Acta Crystallogr. Sect. A

Found. Crystallogr. *64*, 112–122. 10.1107/S0108767307043930.

47. Chai, J.-D., and Head-Gordon, M. (2008). Systematic optimization of long-range corrected hybrid density functionals. J. Chem. Phys. *128*. 10.1063/1.2834918.

48. Vilela Oliveira, D., Laun, J., Peintinger, M.F., and Bredow, T. (2019). BSSE-correction scheme for consistent gaussian basis sets of double- and triple-zeta valence with polarization quality for solid-state calculations. J. Comput. Chem. *40*, 2364–2376. 10.1002/jcc.26013.

49. Frisch, M. J., et al (2016). Gaussian 16 Revision A.03, Gaussian Inc. Wallingford CT at Gaussian Inc. Wallingford CT.

50. Chai, J.-D., and Head-Gordon, M. (2008). Long-range corrected hybrid density functionals with damped atom–atom dispersion corrections. Phys. Chem. Chem. Phys. *10*, 6615. 10.1039/b810189b.